Elliptical Space as the Possible Origin of Matter

Vladimir N. Yershov *

Posted Date: 25 December 2023

doi: 10.20944/preprints202312.0679.v2

Keywords: elliptical space; de Sitter metric; Schwartzschild metric; wormholes; gravitational redshift; type-Ia supernovae

Article

Elliptical Space as the Possible Origin of Matter

Vladimir N. Yershov [1,†]

[1] Formerly Mullard Space Science Laboratory, University College London; vyershov@moniteye.co.uk
* Correspondence: vyershov@moniteye.co.uk
† Current address: 7 Barley Close, Crawley, RH10 6BA U.K.

Abstract: I argue that the main feature of elliptical space – the topological identification of its antipodal points – might be behind some observational facts on both cosmological and microscopic scales. I use calculated distance moduli of type-Ia supernovae, which are commonly regarded as "standard candles" for distance measure in cosmology. These are compared with the observational data collected in a catalogue called "*Pantheon+*". On the microscopic scale I show that a *physical* elliptical space, in which the mathematical connectedness between antipodal points is replaced with physical connections via the Einstein-Rosen bridges (also called "wormholes"), gives rise to sub-particle structures similar to J.A. Wheeler's *geons*. The interactions between these structures leading to their equilibrium configurations can explain the experimentally observed pattern of properties of elementary particles forming the standard model of particle physics. The answer to the question why we have this particular set of fundamental particles might lie in the fundamental properties of elliptical space.

Keywords: elliptical space; de Sitter metric; Schwartzschild metric; wormholes; gravitational redshift; type-Ia supernovae

1. Introduction

W.R. Hamilton (1840) introduced quaternions [1]

$$\begin{aligned} Q &= w + ix + jy + kz; \\ i^2 &= j^2 = k^2 = ijk = -1, \end{aligned} \tag{1}$$

which represent rotation geometry related to elliptical space. Elliptical geometry was first introduced to cosmology by W. de Sitter [2] to replace the hyper-spherical space $\mathbb{S}^3$ of Einstein's first cosmological model [3]. Here I use the term elliptical instead of elliptic to distinguish it from geometry in two- and three-dimensional space, by analogy with hyper-spherical. This is also consistent with de Sitter's terminology in [2].

To achieve consistency with his field equations, Einstein assumed static Riemannian space with constant positive curvature

$$\lambda = R^{-2} \tag{2}$$

for which the spacetime interval is

$$ds^2 = c^2dt^2 - dr'^2 - R^2 \sin^2 \frac{r'}{R}(d\theta^2 + \sin^2\theta d\varphi^2)\,. \tag{3}$$

De Sitter found a new exact solution to Einstein's field equations

$$ds^2 = \cos^2 \frac{r'}{R}c^2dt^2 - dr'^2 - R^2 \sin^2 \frac{r'}{R}(d\theta^2 + \sin^2\theta d\varphi^2) \tag{4}$$

Preprints (www.preprints.org) | NOT PEER-REVIEWED | Posted: 25 December 2023 doi:10.20944/preprints202312.0679.v2

which differs from Einstein's solution (3) by the metric coefficient $g_{tt} = \cos^2 \frac{r'}{R} = \cos^2 \chi$. Here the natural radial coordinate r' is measured by the projective angle χ:

$$r' = R\chi, \tag{5}$$

which is illustrated by Figure 1. De Sitter introduced the coordinate transformation

$$r = R \tan \chi, \tag{6}$$

where r is the projection of natural coordinate r' to Euclidean or Lobachevsky spaces tangential to $\mathbb{S}^3$ at the observer's location o. With respect to projective transformations, de Sitter argued that elliptical space, which is also called projective space, $\mathbb{P}^3$, is preferable for modelling the physical world, rather than $\mathbb{S}^3$. This was also the opinion of Einstein communicated to de Sitter by letter. The main argument was that any two straight lines in $\mathbb{S}^3$ starting from a point intersect again in the antipodal point. By contrast, any two straight lines in elliptical space cannot have more than one point in common. Consequently, when used for projecting natural coordinates to Euclidean (flat) or Lobachevsky (hyperbolic) space, a sphere $\mathbb{S}^3$ covers them twice, which is ambiguous. Whereas the elliptical space $\mathbb{P}^3$ covers them once. This property follows from the structure of elliptical space: the topological identification of its antipodal points corresponding to the projective angle $\chi = \pi$.

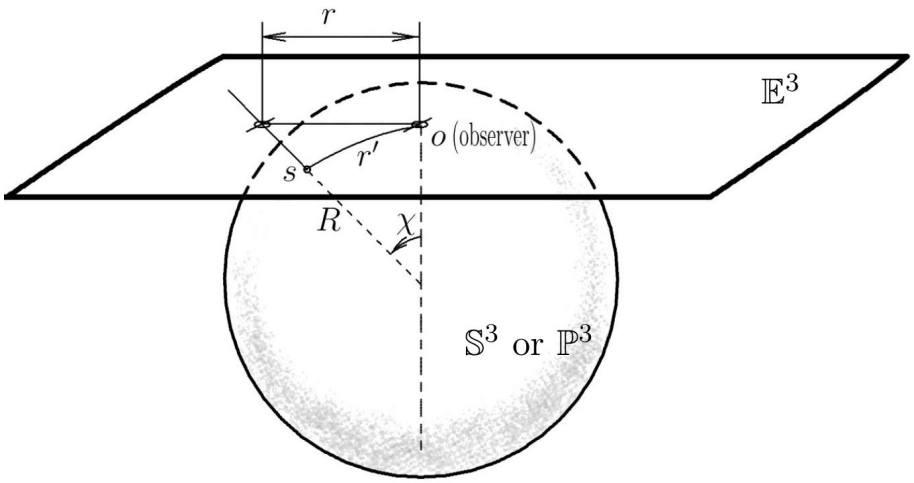

Figure 1. Embedding diagram (one spatial dimension suppressed) depicting spherical $\mathbb{S}^3$ or elliptical $\mathbb{P}^3$ space of constant positive curvature with two antipodal points topologically identified (the dashed connection between two poles). The tangential Euclidean space $\mathbb{E}^3$ at the observer's location o indicates the local coordinate reference frame. Distances r' along the natural spatial coordinate of $\mathbb{S}^3$ are measured by the projective angle χ, with $r' = R\chi$. The corresponding projective distance to the source s in $\mathbb{E}^3$ is $r = R \tan \chi$.

Elliptical space was previously explored by S. Newcomb in 1877 [4] and K. Schwarzschild in 1900 [5]. In the subsequent cosmological models, elliptical space was adopted explicitly by Lemaître [6], Tolman [7], and Robertson [8], then passing tacitly to the current cosmological model ΛCDM (Lambda-Cold-Dark-Matter). Thus, elliptical space is at the root of modern cosmology. However, to the best of the author's knowledge, the possibility of its structure being related to some phenomena or properties of our world has rarely been discussed, aside from a hypothetical possibility of observing our Sun and neighbouring stars or galaxies far away, on the other side of the Universe.

For example, de Sitter himself discussed this possibility in his paper [2]. He wrote: "Space being finite, and the straight line closed, we should, at the point of the heavens opposite the Sun, see an image of the back side of the Sun". It's true that in elliptical space one should see the back side of the Sun

Preprints (www.preprints.org) | NOT PEER-REVIEWED | Posted: 25 December 2023 doi:10.20944/preprints202312.0679.v2

in the opposite direction to the Sun. But this is only half-true because the topological structure of elliptical space provides the theoretical possibility to see *all sides* of the Sun in *all* the directions across the heavens (see the next paragraph for details). The structure of elliptical space was introduced to cosmology for important reasons. Therefore, modern cosmology continues to rely upon it. But the above-cited comment by de Sitter, who was the first to introduce this structure, indicates that even the greatest physicists did not fully realise its significance. Besides seeing our Sun on the whole celestial sphere, one must see in the same way all objects in our neighbourhood, possibly including our Galaxy, and many other galaxies within some distance from us. This is because our neighbourhood is likely to be negligibly small comparing with the distance to our antipodal point. Such is this unusual property of elliptical space which lies at the heart of modern cosmology!

Here, based on two practical examples, I will demonstrate that this property might have important observational consequences. The first example (§ 3.1) deals with the type-Ia supernovae which provide us with well-calibrated distance moduli used in observational cosmology. The discussed physical interpretation of elliptical space is used for calculating theoretical distance moduli and comparing them with observational data.

The second example (§ 3.2) is based on the same physical interpretation of elliptical space, but it is related to the microscopic scale and is used for unveiling the possible origin of the observed pattern of elementary particle species and of their properties described by the standard model of particle physics.

2. Materials and Methods

2.1. De Sitter effect

In Einstein's cosmological model [3], the density of matter $\rho_0 > 0$, with the following relationship between ρ_0 and λ:

$$\kappa\rho_0 = 2\lambda, \tag{7}$$

where $\kappa = 8\pi G/c^2$ is the Einstein constant. The time-related metric coefficient g_{tt} in (3) is unity. So, time is universal for the whole Universe in Einstein's model. By contrast, in de Sitter's model, $\rho_0 = 0$ (there is no matter!) and $\lambda = 3R^{-2}$. The g_{tt} component of the metric (4) is

$$g_{tt} = \cos^2\chi\,, \tag{8}$$

implying that, from the observer's perspective, time at the source's location is dilated, arriving to the complete halt at the maximal distance, at which $\chi = \pi/2$ and $\cos\chi = 0$.

This time dilatation (called the de Sitter effect) causes "the frequency of light-vibrations to diminish with increasing distance from the origin of coordinates. The lines in the spectra of very distant stars or nebulae must therefore be systematically displaced towards the red, giving rise to a spurious positive radial velocity" [2]. This de Sitter's prediction of the cosmological redshift phenomenon was made a decade before its observational discovery in 1927 by Lemaître [6] and in 1929 by Hubble [9].

In the current standard cosmological model, ΛCDM, the cosmological redshift is interpreted in terms of the expanding space paradigm encoded by the Robertson-Walker's time-dependent scaling factor $a(t)$ in the Friedmann-Lemaître-Robertson-Walker (FLRW) metric [6,8,10,11], with no possible alternatives. The Hubble diagram based on the FLRW metric fits pretty well the observational distance moduli from the *Pantheon+* catalogue of 1701 type-Ia supernova data.

2.2. Luminosity distances.

Luminosity distances and distance moduli based on the de Sitter effect and the metric coefficient (8) do not match observational data. For example, the comparison of the ΛCDM-model with the observational data from [13] gives a pretty small value of the goodness-of-fit parameter $\chi^2_{\Lambda\mathrm{CDM}} = 901.6$, whereas a similar parameter for de Sitter's model is very large (many thousands). This comparison is

 doi:10.20944/preprints202312.0679.v2

made by using the ΛCDM parameters from [13]: $\Omega_m = 0.334$ and $H_0 = 73.6\,\mathrm{km\ s^{-1}\ Mpc^{-1}}$, assuming a flat cosmology with $\Omega_k = 0$.

For devising a better relationship between luminosity distances and redshifts of remote sources within the elliptical space framework, one can resort to the main property of this space – the topological connectivity between its antipodal points.

The connectivity of points separated by some distance can be viewed as their short-circuiting, which is sometimes associated with quantum entanglement of subatomic particles separated by large distances [14] or even with the possibility of instantaneous travels between remote regions of space [15]. A general-relativistic description of such a feature was discovered in 1935 by Einstein and Rosen [16], and it is called the Einstein-Rosen bridge or, more frequently, a "wormhole".

Morris, Thorne & Yurtsever [17] found that wormhole creation must be accompanied by extremely large energies aka spacetime curvatures. This means that wormholes are likely to be microscopic, on a scale-length of the order of the Planck-Wheeler length, $\ell_\mathrm{P} = \sqrt{G\hbar/c^3} = 1.62 \cdot 10^{-33}\,\mathrm{cm}$. A static wormhole can be described by the Schwarzschild metric (in spherical coordinates r, θ, ϕ):

$$ds^2 = g_{tt}c^2dt^2 - g_{rr}dr^2 - r^2(d\theta^2 + \sin^2\theta d\varphi^2)\,, \tag{9}$$

which is what we need for calculating redshifts in elliptical space if the mathematical connectivity of its antipodal points is physically interpreted as the connectivity via microscopic wormholes. The metric coefficients g_{tt} and g_{rr} of the Schwarzschild metric

$$g_{tt} = 1 - \frac{r_g}{r} \quad \text{and} \quad g_{rr} = g_{tt}^{-1} \tag{10}$$

are distinct from those of the de Sitter metric (4). Thence, in this approach, the redshifts of remote sources are not due to the de Sitter effect, but due to the gravitational redshift corresponding to the metric coefficient g_{tt} in (10). So, in addition to the initial free parameter R, there is another parameter r_g corresponding to the Schwarzschild radius, which is unknown.

Originally, the Schwarzschild metric (9) was devised for asymptotically flat spacetimes ($R^{-2} \to 0$ as $r \to \infty$). In our case, finite values of R are allowed, so we keep R as a free parameter. For this reason, in our calculations we need a modified Schwarzschild metric residing in a curved space. Such metric was devised in 1939 by R.C. Tolman [18], who proposed a general method for finding exact solutions of Einstein's field equations. Among various solutions described by him in [18], the suitable one for our case is the solution No.II with the Swarzschild-de Sitter (SdS) metric. It differs from the Schwarzschild solution (9) by an additional term in the metric coefficient g_{tt}, which accounts for the possibility of finite values of R:

$$g_{tt} = 1 - \frac{r_g}{r} - \frac{r^2}{R^2}\,, \tag{11}$$

the metric coefficient related to radial-coordinates being $g_{rr} = g_{tt}^{-1}$, like in (9).

We assume that two wormhole's throats are located at two antipodal points separated by a very large distance from each other ($\chi = \pi$). Yet they are also short-circuited via a microscopic wormhole structure (in Figure 1 this is shown as a connection between the north and south poles marked with a dashed line). The observer is located near one of the throats (called hereafter the near-throat), the source being somewhere in between the observer and the far-throat of the observer's antipodal-point.

In Figure 1, distances r and r' are measured from the origin at the observer's location (o) towards a remote source (s). As we know from the de Sitter's model case, this measurement does not lead to an agreement with observations. One can subdue this problem by transferring the origin of coordinates to the observer's antipodal point. In this new set-up, the distances to the source (r_s) and observer (r_o) are measured from the wormhole's far-throat, which is unusual, but we shall see that this provides a better agreement between the model and observations (hereinafter, we drop the prime indices previously used for denoting quantities in the natural space $\mathbb{S}^3$).

Preprints (www.preprints.org) | NOT PEER-REVIEWED | Posted: 25 December 2023 doi:10.20944/preprints202312.0679.v2

A diagram corresponding to this alternative choice of the origin is presented in Figure 2 where the entire sphere $\mathbb{S}^3$ is conformally mapped to the Poincaré disk.

For clarity, the observer's location (o) in this diagram is shown slightly shifted from the center of the Poincaré disk. The antipodal point of the disk's center is transformed in this map in such a way that it appears as the disk's circumference (the outermost dash-dotted circle in Figure 2). In the three-dimensional space $\mathbb{S}^3$, this circle corresponds to a 2-sphere $\mathbb{S}^2$ surrounding the observer at a very large distance (πR) from the observer.

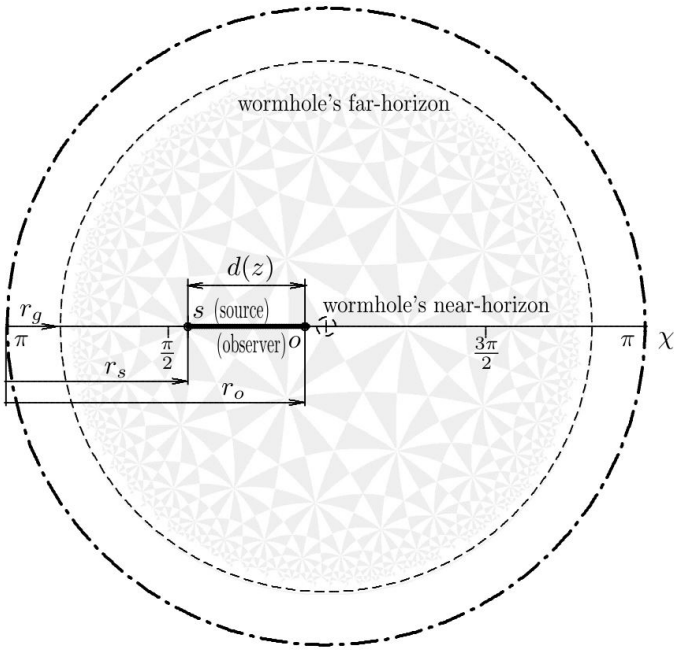

Figure 2. Poincaré disk illustrating the concept of the spherical symmetry of wormhole far-throats around each point in elliptical space. The disk spans the whole of the $\mathbb{S}^3$ sphere, the central point of the disk (the centre of the wormhole's near-throat) being near the observer's location o. A small dashed circle around the central point denotes the event horizon of the near-throat, and the larger dashed circle denotes the corresponding event horizon of the wormhole's far throat. The distances r_s, r_o and r_g are measured from the centre of the far-throat (the outer dot-dashed circle).

And yet, it is a zero-size point near the observer – see our comments in Section 1 about the unusual property of elliptical space, which makes the objects in the vicinity of the observer to be visible in all directions across the celestial sphere. One would need to keep in mind that this circle (a sphere $\mathbb{S}^2$) and the central point of the disk are not distinguished in elliptical space.

In concordance with our choice of the origin of coordinates, any distance is now measured from this 2-sphere towards the source (r_s) or towards the observer (r_o). These two distances are indicated in Figure 2 by the arrows from the left edge of the diagram. Our purpose here is to find a relationship between the source redshift (z) and the source-to-observer distance (d):

$$d(z) = r_o - r_s \,. \tag{12}$$

Any point slightly offset from the center of the Poincaré disk has its corresponding antipodal sphere at a small distance from the disk border towards the interior of the disk. For example, if we draw a small 2-sphere around the center of the disk near the observer (a small central dashed circle in the scheme which denotes the wormhole's near-throat), then its corresponding antipodal 2-sphere (the wormholes far-throat) will be very large, which is shown in Figure 2 as a large dashed circle at some distance r_g from the disk border. Although the observer is nearby and *outside* of this small sphere, yet

Preprints (www.preprints.org) | NOT PEER-REVIEWED | Posted: 25 December 2023 doi:10.20944/preprints202312.0679.v2

it is *inside* of it because the antipodal image of this sphere completely surrounds the observer at far distances.

Spherical symmetry.

An essential aspect of this construct is its spherical symmetry for any arbitrary location. This follows from the topology of elliptical space. When looking at the near-throat of a microscopic wormhole, the observer localises it within a very narrow (nearly zero) solid angle of $\sim 10^{-33}$ cm across. But when the observer looks at the far throat of the same microscopic wormhole, the solid angle spans 4π steradians (a sphere around the observer), as we have discussed above.

The remote horizons corresponding to locations within some vicinity of the observer are at extremely large distances from the observer. From the observer's perspective, this neighbourhood region might appear large, including some nearby galaxies of even clusters of galaxies. But this size is likely to be negligible as compared with the distances to the remote horizons. Therefore, the average collective horizon around any point of space must be almost ideally spherically symmetric, thus, making all points of space equivalent to each other.

Redshift-distance relationship.

In our set-up shown in Figure 2 there are two unknown distances, r_o and r_s. The latter can be replaced with the source-to-observer distance (12). The gravitational radius r_g and the global radius R are also unknowns, as was mentioned before. So, in total, our model has three free parameters, r_o, r_g and R, to be determined by using observational data.

Both source and observer are located within the Schwartzschild-de Sitter metric (9) with its redshift-defining coefficient (11). So, the source's redshift with respect to the observer is

$$z = \sqrt{\frac{g^o_{tt}}{g^s_{tt}}} - 1 \tag{13}$$

or, by taking into account (11),

$$(z+1)^2 = \frac{1 - \frac{r_g}{r_o} - \frac{r_o^2}{R^2}}{1 - \frac{r_g}{r_s} - \frac{r_s^2}{R^2}} \,. \tag{14}$$

At this point, we can define the parameter r_g as unit distance for measurements, $r_g = 1$. Later on, it can be converted to some common distance units, like Mpc. Thus,

$$(1+z)^2 = \left(1 - r_o^{-1} - r_o^2 R^{-2}\right)\left(1 - r_s^{-1} - r_s^2 R^{-2}\right)^{-1} \,. \tag{15}$$

From (12)

$$r_s = r_o - d \,, \tag{16}$$

which gives

$$(r_o - d)^{-1} = 1 - (1 - r_o^{-1} - r_o^2 R^{-2})(1+z)^{-2} - (r_o - d)^2 R^{-2}. \tag{17}$$

Then the source-to-observer distance reads

$$d = r_o - \left[1 - (1 - r_o^{-1} - r_o^2 R^{-2})(1+z)^{-2} - (r_o - d)^2 R^{-2}\right]^{-1} \,, \tag{18}$$

which is a recursive expression [in units of r_g] for finding the source-to-observer distance as a function of the source redshift. It has to be multiplied yet by the scaling factor $(1+z)^2$ in order to obtain the source luminosity distance:

$$d_L(z) = d\,(1+z)^2 \,, \tag{19}$$

Preprints (www.preprints.org) | NOT PEER-REVIEWED | Posted: 25 December 2023 doi:10.20944/preprints202312.0679.v2

with one of the $(1+z)$-factors accounting for the loss of luminosity due to the cosmological redshift z and also for the lower rate at which the photons reach the observer because of the cosmological time dilatation caused by the non-unit metric coefficient g_{tt}, and another accounting for the photon path distortion (the g_{rr} coefficient in the Schwarzschild-de Sitter metric). This relationship can be used for determining the unknown parameters of our model by fitting the theoretical distance moduli

$$\mu = 5 \log d_L + 25 \tag{20}$$

(in stellar magnitudes) to the observational distance moduli of type Ia supernovae. The numerical coefficients in (20) correspond to the luminosity distances d_L expressed in Mpc.

3. Results

3.1. Cosmological scale

By using formulae (18), (19) and (20) for the SdS metric one can calculate the theoretical luminosity distances d_L^{SdS} and distance moduli μ^{SdS} corresponding to the redshifts of the type-Ia supernova sources from the *Pantheon+* catalogue. The comparison of these distance moduli with the observational data from *Pantheon+* is presented in Figure 3. The fit of our theoretical model to the observational data is implemented by minimising the Pearson χ^2 criterion for three free parameters of the model, r_o, R and r_g. The minimum of $\chi^2_{\mathrm{SdS}} = 887.6$ corresponds to the following parameter values:

$$\begin{aligned} r_o - 1 &= (9.91^{+0.16}_{-0.15}) \cdot 10^{-8}\,, \\ R &= (1.076^{+\infty}_{-0.023}) \cdot 10^{5}\,, \\ r_g &= (2.130 \pm 0.003) \cdot 10^{10}\ [\mathrm{Mpc}]\,, \end{aligned} \tag{21}$$

the first two parameters, r_o and R, being in units of r_g. The tolerance interval for the parameter R turns out to be only a half-interval (with no upper bound) because any value above $R = 1.076 \cdot 10^5$ provides an equally good fit of the model to the observational data.

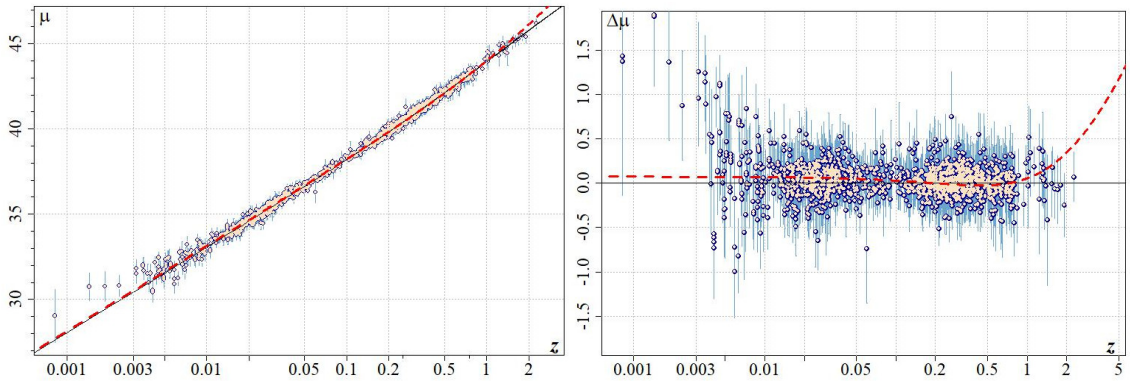

Figure 3. *Left:* comparison of theoretical distance moduli μ (the red and black curves) with the observational distance moduli of 1701 type-Ia supernovae from the Pantheon+ catalogue (the salmon-colour points). The dashed red curve corresponds to the model based on the Schwarzschild-de Sitter metric, while the solid black curve is the reference corresponding to the standard ΛCDM cosmological model. *Right:* The same data in detail, plotted in the form of the residuals $\Delta\mu$ with respect to the ΛCDM-reference, which is thus the horizontal line at $\Delta\mu = 0$. The abscissae in both plots correspond to the source redshifts z.

The salmon-colour points in Figure 3 correspond to the observational data from *Pantheon+* [13]. The SdS theoretical distance moduli for the minimum of χ^2_{SdS} are plotted as the red dashed curve, and the ΛCDM fit from [13] is shown as the black curve.

Preprints (www.preprints.org) | NOT PEER-REVIEWED | Posted: 25 December 2023 doi:10.20944/preprints202312.0679.v2

By comparing the previously estimated goodness-of-fit parameter $\chi^2_{\Lambda\mathrm{CDM}} = 901.6$ for ΛCDM model with $\chi^2_{\mathrm{SdS}} = 887.6$ for the model based on the Schwarszchild-de Sitter metric, one can say that the latter provides an equal or better fit to the observational data. That is, for building Hubble diagrams within the redshift range covered by the *Pantheon+* data these two models are equivalent.

3.2. Microscopic scale

Both cosmological models discussed in § 2 correspond to an empty space, with matter density $\rho_o = 0$. However, the first of them, based on the de Sitter metric (§ 2.1) is internally inconsistent because it predicts a cosmological redshift of remote sources of light, whereas there is no matter and hence no sources of light corresponding to this solution.

The second model (§ 2.2) is also based on an empty space. But this space is endowed with the Szchwarzschild-de Sitter metric of its topological features (microscopic wormholes). So, there is a difference between the first and second empty-space solutions: the first describing a truly empty space, whereas the space corresponding to the second solution contains microscopic entities which can carry energy and which, thus, can be associated with microscopic particles, giving origin to what we understand as matter.

3.2.1. Wheeler's wormhole particles.

One of the first physicists to embrace this idea was J.A. Wheeler [19] who discussed the possibility of an electromagnetic disturbance being capable of holding itself together by its own gravitational force because a disturbance contains energy and hence mass. Wheeler called these stable structures *geons* as an abbreviation for a "gravitational-electromagnetic entity".

At that point, Wheeler arrived at the idea of space multi-connectedness via wormholes. He envisaged that there is no discontinuity of lines of force of an electric charge at the origin. Instead, these lines continue through the throat of a microscopic wormhole, as shown in Figure 4, which is redrawn (with some modifications) from Wheeler's 1955 Physical Review paper [19]. Two wormhole throats of the $\sim 10^{-33}$ cm size are connected by a tunnel, which allows the lines of forces being continuous, so each throat appears as a charge.

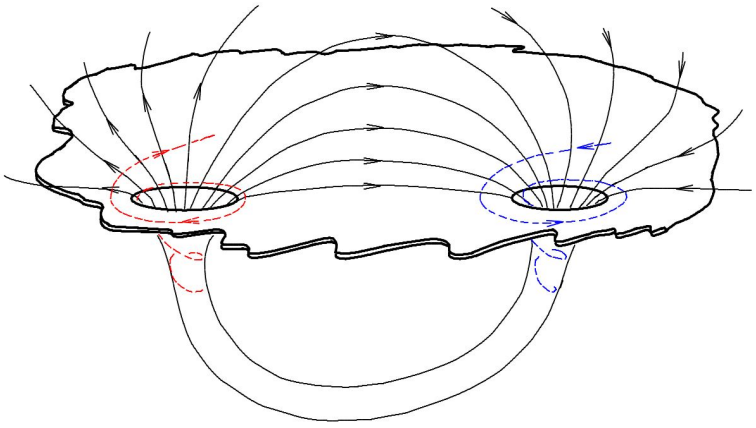

Figure 4. Embedding diagram depicting Wheeler's concept of microscopic wormholes as electric charges – redrawn from his 1955 Physical Review paper [19] to illustrate his idea of the continuity of electric force lines. The picture is modified by adding vorticity force lines (the red and blue spiral dashed curves).

According to this picture, matter particles might be dislocations of space in the form of wormholes – that is, matter particles are "made" of space. This is in line with de Sitter's idea of an empty universe because with the Schwarzschild-de Sitter metric of wormholes populating the whole space, as described in § 2.3, the universe remains empty but yet it contains "matter" particles formed of space

Preprints (www.preprints.org) | NOT PEER-REVIEWED | Posted: 25 December 2023 doi:10.20944/preprints202312.0679.v2

itself. As Wheeler put it: "there is nothing in the world except empty curved space" [20]. That is why he characterised general relativity as a theory that is capable "not only to account for the fields produced by bodies, and the motions of bodies, but even to explain why there should be bodies" [19].

3.2.2. Concept of tripolarity.

Of course, none of the Wheeler's simple electric charges depicted in Figure 4 could be accepted as a realistic model of a standard elementary particle, like the electron, because the electron is known to be more complex by possessing a variety of properties (such as spin, magnetic moment, charge-parity symmetry etc.) rather than having just the property of carrying an electric charge. Therefore, the only way of interpreting the Wheeler's simple wormholes from Figure 4 as matter particles would be by regarding them as the simplest possible constituents of the electron and other more complex particles observed in Nature.

This is the main point of the hypothetical framework which I discuss here, arguing that *the physical* elliptical space whose every point is populated with a microscopic wormhole (like those from Figure 4) might be behind the origin of the observed variety of fundamental particles, which are theoretically well described by the standard model of particle physics. But the standard model is not aimed at answering the question why do we have this particular set of particles and not something else.

In the standard model of particle physics, the fundamental particles are point-like entities, having no structure. However, there exists a pattern observed in the properties of the standard-model particles: the particles species are repeated trice, with their properties (except mass) being exactly the same in three families of the fundamental fermions. The existence of a pattern suggests that there must be a deeper structural layer (or layers) behind this pattern.

A microscopic wormhole possesses a minimal set of properties, which makes this object suitable for modelling hypothetical structural elements of more complex matter particles. Besides its electric charge, which can be positive or negative (corresponding to the outflow and inflow of the force lines), there is a property corresponding to the vorticity of force lines, which is indicated in Figure 4 by the red and blue dashed curves spiraling in and out of the wormhole throats.

The inflow/outflow of the force lines corresponds to the $[-/+]$ symmetry of a conventional electric charge, allowing the attraction/repulsion between unlike-/like-charges. This U(1) symmetry has a very limited range of possibilities for structure formation. The vorticity of the field adds the necessary complexity to the attraction-repulsion pattern between wormhole particles, which allows a larger number of their possible equilibrium configurations.

The embedding diagram in Figure 4 is unavoidably two-dimensional. Consequently, there are only two possible vorticity signs shown – clockwise (red) and anticlockwise (blue). In the natural three-dimensional space, the number of possible rotations is three, in accordance with rotational geometry represented by quaternions (1). So, the vorticity of the field is triplicate, which can be called *tripolarity* – by analogy with the bipolarity $[+/-]$ of conventional charges. Usually, the polarities of tripolar fields are denoted by three complementary colours – red, green and blue or [r,g,b]. That is why I have used two of these colours (red and blue) in Figure 4 to denote the particle colour charges.

The notion of colour charge was introduced by O.W. Greenberg in 1964 [21], whose study was related to strong interactions between hadrons. The strong-like symmetry SU(3) of wormholes' colour charges is not exactly the same as what is currently used in quantum chromodynamics, but the analogy is obvious. The bipolar symmetry $[+/-]$ of the positive and negative charges is preserved here, so the combined symmetry of the resulting *chromoelectric* field is $U(1)\times SU(3)$, which is relatively simple, but which is complex enough to guarantee the emergence of a unique set of structures based on colour fields.

Preprints (www.preprints.org) | NOT PEER-REVIEWED | Posted: 25 December 2023 doi:10.20944/preprints202312.0679.v2

3.2.3. Chromoelectric field.

Let the basic wormhole particle be the source of a chromoelectric field $\mathbf{E}_c$ with two components:

$$\mathbf{E}_c = (\mathbf{E}, \mathbf{C}) \tag{22}$$

(ignoring for the moment the associated chromo-magnetism), where $\mathbf{E}$ is the component with two polarities $[+/-]$, similar to the conventional electric field, and $\mathbf{C}$ is the tripolar (colour) component whose three polarities can be denoted as [r,g,b]. Then a wormhole particle carrying different colour charges can be denoted as r^+, g^+, b^+ or r^-, g^-, b^-; the superscript indicating the polarity sign of the electric charge (so, there is a variety of six of them). We can assume a unit value for the charge of this basic particle, thus, defining the charge unit $[q_\circ]$ for our model. As the field (22) is spherically symmetric, we shall use the following one-dimensional functional form for its components:

$$\begin{aligned} C(r) &= \varkappa \exp(-\kappa r^{-1}), \\ E(r) &= -C'(r) = -\varkappa r^{-2} \exp(-\kappa r^{-1}), \end{aligned} \tag{23}$$

where r is the radial distance from the wormhole's centre. The coefficient $\varkappa = \pm 1$ denotes here the polarity of the field; it must be chosen such as to reproduce the known pattern of attraction and repulsion between different charges (i.e., opposite electric- or colour-charges attract each other and like-charges repel); κ is the range coefficient, which we shall set to unity in order to avoid using free parameters.

The functional forms (23) of two components of the chromoelectric field (22) mimic the known electric and strong fields: the electric-like component $E(r)$ decays according to the inverse-square law, and the strong-like component $C(r)$ remains almost constant at far distances. Besides its tripolarity, the field (22) differs from the conventional electric field by having no singularity at the origin (which is the property of a wormhole).

Of course, like in the case of the conventional electric field, the energy of the field (22) integrated over the entire space is divergent, because its colour components in the vector $\mathbf{C}$ remain almost constant at far distances. However, the energy/mass of a system containing *all three* complementary (unlike) colour-charges is finite, owing to the mutual cancellation of three opposite colour-fields. This reproduces, as required, the confinement of colour-charges within colour-neutral systems. Such a system can be called *a tripole* – by analogy with conventional dipoles formed of particles with two unlike electric charges. If all three (r, g and b) components share the same spatial origin, the cancellation

$$\mathbf{C}^{\mathrm{r}}(r) + \mathbf{C}^{\mathrm{g}}(r) + \mathbf{C}^{\mathrm{b}}(r) = 0 \tag{24}$$

is exact for any r, corresponding to the 100% mass defect of the colour-field components, and one can treat such a system as if it were a system of three conventional electric charges. If the field sources are separated from each other (even slightly), the field around them becomes colour-polarised, as illustrated by Figure 5, where three complementary graphical colours are used to visualise three complementary colour fields. Here the white graphical colour corresponds to the colour-neutral field at far distances from the tripole systems. The excess of colours in the neighbourhood of each tripole indicates the colour-polarisation of the field.

Preprints (www.preprints.org) | NOT PEER-REVIEWED | Posted: 25 December 2023 doi:10.20944/preprints202312.0679.v2

Figure 5. Polarisation of the cromoelectric field (23) in the vicinity of tripole systems, each being formed of three complementary (unlike) colour-charges.

In practical terms, one can calculate the superposition (24) by analogy with the superposition of conventional electric fields of opposite polarities $\mathbf{E}^{+}$ and $\mathbf{E}^{-}$, using a colour space $\{\mathrm{r},\mathrm{g},\mathrm{b}\}$ with three degrees of freedom for each of the spatial coordinates $\{x,y,z\}$ instead of two degrees of freedom $\{+,-\}$ that are used for conventional electric fields.

A diagram for colour-vector summation is shown in Figure 6 for three colour-components C^{r}, C^{g} and C^{b} of a field $\mathbf{C}$ along one of the spatial coordinates, either x, y or z, i.e. for either of the sets of quantities $\{C^{\mathrm{r}}_x, C^{\mathrm{g}}_x, C^{\mathrm{b}}_x\}$, $\{C^{\mathrm{r}}_y, C^{\mathrm{g}}_y, C^{\mathrm{b}}_y\}$ or $\{C^{\mathrm{r}}_z, C^{\mathrm{g}}_z, C^{\mathrm{b}}_z\}$. In this particular example, the amplitudes of all three components, are chosen to be different, so that the resulting superposition (Σ) is not colour-neutral. It contains two non-zero colour-components Σ^{r} and Σ^{g}, the third component (Σ^{b}) vanishing because in this example the magnitude of C^{b} in the colour-vector $\mathbf{C}$ is smaller than the magnitudes of C^{r} and C^{g}. In principle, it is also possible that two or all three components of Σ vanish, if, correspondingly, two or three of the quantities $\{C^{\mathrm{r}}, C^{\mathrm{g}}, C^{\mathrm{b}}\}$ are equal to each other.

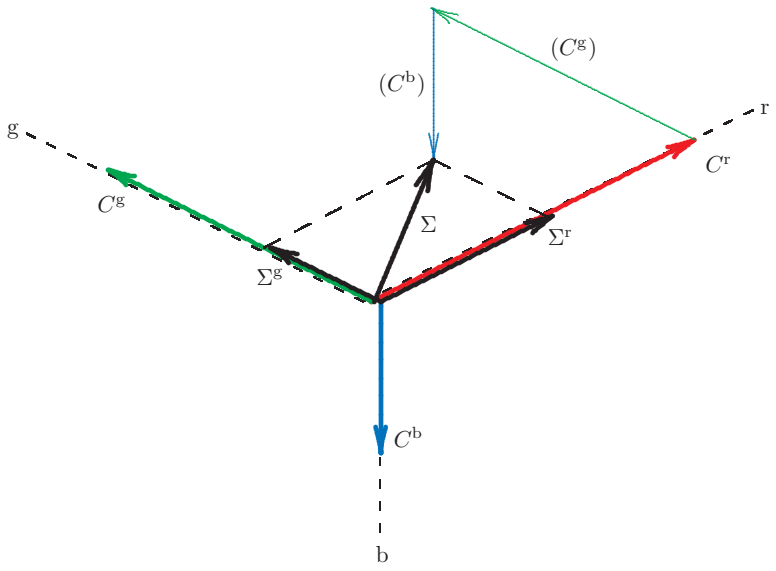

Figure 6. Superposition of colour-field components C^{r}, C^{g}, C^{b}, in the colour space $\{\mathrm{r},\mathrm{g},\mathrm{b}\}$ for one of the spatial coordinates (either x, y or z). In this particular example, the resulting field Σ has only two colour-components, Σ^{r} and Σ^{g}, the component Σ^{b} being equal to zero due to the smaller amplitude of the b-component C^{b} in the initial colour vector $\mathbf{C}$.

Preprints (www.preprints.org) | NOT PEER-REVIEWED | Posted: 25 December 2023 doi:10.20944/preprints202312.0679.v2

3.2.4. Tripoles.

The potential corresponding to the field (23) of a composite system formed of like-charged particles with unlike colours is

$$V(r) = (1 - r)\exp(-r^{-1}) - \mathrm{Ei}(-r^{-1}), \tag{25}$$

which is a double-well potential (Figure 7) determining structure formation in composite systems by having a number of local minima. This is similar to the cluster-formation scheme in molecular dynamics [22,23]. The only difference is that one needs to take care of the tripolarity of the involved fields. These local minima give rise to a unique set of allowed spatial structures, the simplest of which is the charged colour tripole formed of three mutually-complementary colour charges with one of the electric polarities, $+$ or $-$.

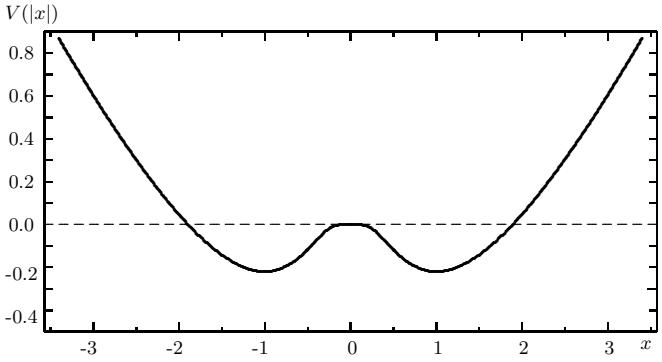

Figure 7. One-dimensional slice of the double-well potential (25) corresponding to the chromoelectric field (23). The half-separation between wells defines the distance unit for this field, $l_\circ = 1$.

This potential is self-calibrating because it establishes the length, time and energy scales by the separation between the potential wells (length), the frequency of a test-particle oscillations in the inverted potential barrier (time) and the barrier height (energy). For our calculations we shall define the length unit, $l_\circ = 1$, to be the half-separation the between potential wells. This distance corresponds to the equilibrium between two like-charged particles with unlike colours. The unit of mass, $m_\circ = 1$, can be defined by considering the momentum density $\mathbf{p}$ of the field, following the approach proposed by Lorentz [24] and further developed by Born[25,26], Dirac [27], Landau [28] and other authors [29]:

$$\mathbf{p} = \mathbf{S}/c^2 = \frac{1}{4\pi c}[\mathbf{E}_c \times \mathbf{H}_c], \tag{26}$$

where $\mathbf{S} = \frac{c}{4\pi}[\mathbf{E}_c \times \mathbf{H}_c]$ is the Poynting vector and c is the critical speed. With

$$\mathbf{H}_c = \frac{[\mathbf{v} \times \mathbf{E}_c]}{c\sqrt{1 - v^2/c^2}},$$

the momentum density is

$$\mathbf{p} = \frac{[\mathbf{E}_c \times [\mathbf{v} \times \mathbf{E}_c]]}{4\pi c^2\sqrt{1 - v^2/c^2}} = \frac{(\mathbf{v} \cdot \mathbf{E}_c^2 - \mathbf{E}_c(\mathbf{v} \cdot \mathbf{E}_c))}{4\pi c^2\sqrt{1 - v^2/c^2}}. \tag{27}$$

If the z-axis is directed along the velocity vector ($v = v_z$, $v_x = v_y = 0$), the total momentum will be

$$\mathbf{P} = \frac{v}{4\pi c^2\sqrt{1 - v^2/c^2}} \int_{\mathcal{V}} ((\mathbf{E}_c)_x^2 + (\mathbf{E}_c)_y^2)\, d\mathcal{V}, \tag{28}$$

Preprints (www.preprints.org) | NOT PEER-REVIEWED | Posted: 25 December 2023 doi:10.20944/preprints202312.0679.v2

where $\mathcal{V}$ is the volume of integration (presumably the whole space). In the spherically-symmetric case $d\mathcal{V} = 4\pi r^2 dr$,

$$(\mathbf{E}_c)_x^2 = (\mathbf{E}_c)_y^2 = (\mathbf{E}_c)_z^2 = \frac{1}{3}\mathbf{E}_c^2,$$

$$(\mathbf{E}_c)_x^2 + (\mathbf{E}_c)_y^2 = \frac{2}{3}\mathbf{E}_c^2,$$

so that

$$\mathbf{P} = \frac{v}{4\pi c^2\sqrt{1 - v^2/c^2}} \int_0^\infty \frac{2}{3}\mathbf{E}_c^2\, 4\pi r^2\, dr. \tag{29}$$

Then the mass of the field can be defined as

$$m = \frac{2}{3c^2} \int_0^\infty \mathbf{E}_c^2\, r^2\, dr. \tag{30}$$

For a single colour-charge this integral diverges. Therefore, we need to define the unit mass as one-third of the mass of the colourless three-component system for which this integral is finite. Such a system can be called *the tripole* and denoted as $Y^+ = \mathrm{r}^+\mathrm{g}^+\mathrm{b}^+$ or $Y^- = \mathrm{r}^-\mathrm{g}^-\mathrm{b}^-$. Its components are like-charged, and their centres coincide at the origin. In such a system, the three diverging colour-fields (24) are mutually cancelled exactly for the whole range of distances r, leaving just a single convergent term under the integral sign. Then, the field of the tripole Y is $\mathbf{E}_c^Y = 3\mathbf{E}$, and

$$m_\circ \stackrel{\text{def}}{=} \frac{1}{3}m_Y = \frac{1}{3}\cdot\frac{2}{3c^2}\int_0^\infty (3\mathbf{E})^2 r^2\, dr = \frac{2}{c^2}\int_0^\infty r^{-2}\exp(-2r^{-1})\, dr = \frac{1}{c^2} \tag{31}$$

because

$$\int_0^\infty r^{-2}\exp(-2r^{-1})\, dr = \frac{1}{2}.$$

We can define the speed unit to be equal to the critical speed: $v_\circ = c = 1$. The time unit $t_\circ$ is, thus, such that $v_\circ t_\circ = l_\circ$. These units define any other necessary unit.

The charge of the tripole Y is $q_Y = \pm 3q_\circ$. Its mass, m_Y, is equal to $3m_\circ$, which is the exact value if the centres of its three components coincide at the origin. Figure 7 shows that the stationary-state equilibrium at the origin ($x = 0$) is unstable, so the tripole is more likely to be found in its ground state with its three constituents separated from each other by distance $l_\circ$. In this case, its colour-fields $\mathbf{C}$ are cancelled only partially (the field is polarised), which gives some extra mass to the system, so $m_Y > 3m_\circ$. The mass excess m_{ex} can be calculated by using the integral (30). The mass excess calculated for the symmetrical Y-shaped tripole is shown in Figure 8 as a function of the tripole's radius R_Y. For $R_Y = l_\circ/\sqrt{3}$ this system has a mass excess of approximately 5.51 $m_\circ$ per colour charge.

Preprints (www.preprints.org) | NOT PEER-REVIEWED | Posted: 25 December 2023 doi:10.20944/preprints202312.0679.v2

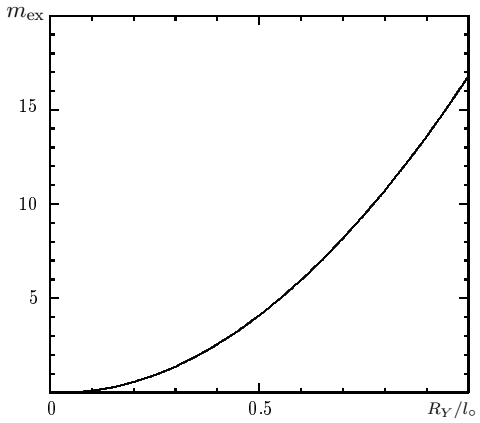

Figure 8. Mass excess (m_{ex}) of the tripole system Y calculated for its symmetrical configuration as a function of tripole's radius R_Y in units of $m_\circ$ per particle.

3.2.5. Strings of tripoles.

Due to the colour-polarisation of the tripole's fields, different tripoles can interact with each other via the van der Waals forces. For example, two like-charged tripoles Y^+Y^+, separated by a large distance are attracted to each other because the strong-like fields of their colour-charge constituents are not fully cancelled. The residual strong-like forces of one tripole act on another tripole and vice versa. The repulsion between their electric like-charges is negligible at large distances. So, tripoles separated from each other by a large distance will be accelerated towards each other until reaching the distance of equilibrium, when the attractive van der Waals force of their residual colour fields is equal to their electric repulsion force. Such a string will oscillate around its equilibrium point. One can calculate the equilibrium distance between two tripoles by using formulae (23) and (25), which is illustrated by Figure 9.

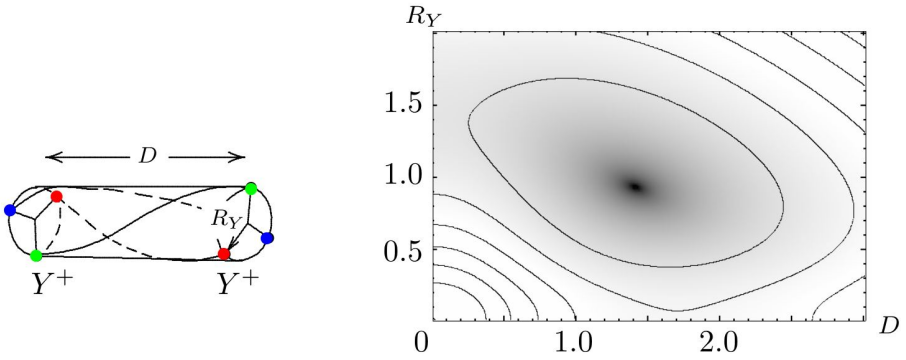

Figure 9. Calculation of the equilibrium distance between two like-charged tripoles Y^+/Y^+ bound together by their residual strong-like (colour) field. This distance corresponds to the minimum of the potential energy of this system (the darker region on the potential-energy map shown on the right panel). The varied parameters for finding the potential energy are the tripole's radius R_Y and the separation D between the tripoles (indicated on the left panel).

A geometrical scheme used for this calculation is shown on the left panel of Figure 9. The potential energy for this case is calculated by varying two parameters: the tripole's radius R_Y and the separation D between two tripoles (indicated on the scheme). The corresponding two-dimensional energy map is shown on the right panel. The scales of the horizontal and vertical axes (D and R_Y, respectively) are expressed in units of $l_\circ$, the half-separation between the wells of the equilibrium potential shown in Figure 7. The equilibrium is reached for $D \approx 1.4$ and $R_Y \approx 1$, around which the system will oscillate. There is a third parameter to vary, which is the phase angle ϕ corresponding to tripole rotations

Preprints (www.preprints.org) | NOT PEER-REVIEWED | Posted: 25 December 2023 doi:10.20944/preprints202312.0679.v2

with respect to each other. But for simplicity we have fixed it to the value $\phi = \pi$, which is likely to correspond to the equilibrium.

The electron.

The chromofield around the system of two like-charged tripoles Y^+Y^+ remains polarised. Thence, any other like- or unlike-charged tripoles will be attracted to the system. When a third like-charged Y^+-component interacts with a two-component string Y^+Y^+, it is attracted to both ends of this string, thus, closing the string into a loop. The equilibrium phase angles in this case are $\phi = \pi/3$, which are maintained if three Y^+-components of this system rotate altogether about their common loop-closed axis (the dashed curve in Figure 10).

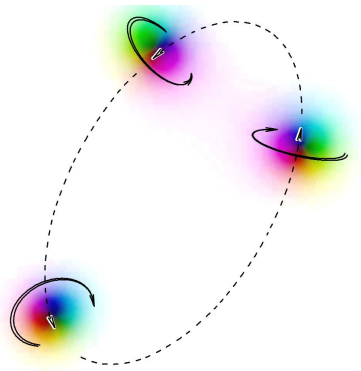

Figure 10. A three-component system of like-charged Y-particles (tripoles) is ring-closed, with the common axis indicated by the dashed curve. The orientation of each tripole with respect to the others in this system corresponds to the phase angle $\phi = \pi/3$. The tripoles move along this axis, as indicated by the arrows, and yet spinning about it, as indicated by the arrowed arcs.

This spinning motion induces a toroidal magnetic field along the loop. Due to the corresponding Lorentz force, the spinning tripoles will be pushed into their orbital motion. This orbital motion along the ring-closed axis generates a poloidal magnetic field of the system, contributing to the spin of these charges about this axis, and so forth, until the constituents of the system reach their maximal available speed. Such a dynamo mechanism for generating a self-contained magnetic field is studied in detail in astrophysics [30,31] and solar physics [32,33]. It is also used for stabilisation of toroidal plasma flows in tokamak fusion reactors [34–36]. We are not going to explore this motion here. What is important is that the ring-closed configuration of tripoles has the lowest possible energy among other configurations and the highest binding energy. So the system $e^+ = Y^+Y^+Y^+$ or $e^- = Y^-Y^-Y^-$ must be stable.

The colour-currents due to the motion of each individual colour-charge in this system are helices which by their closure make a π-twist around the ring-closed axis with either clockwise or anticlockwise winding (these shapes are known as Smale-Williams curves). Such a twisting dislocation of the phase is a conserved quantity called topological charge [37] or dislocation index, which has a sign corresponding to the winding direction (clockwise or anticlockwise) and the magnitude related to the winding number per 2π-orbit path. In these terms, the π-phase shift of the currents in the structure $Y^+Y^+Y^+$ corresponds to a topological charge $S = \pm\frac{1}{2}$, identifiable also with the internal angular momentum (spin) of the system.

A scheme of these trajectories for the case of the anticlockwise winding of the internal colour-currents of the system is presented on the left panel of Figure 11. The right panel of this Figure shows the chromoelectric potential of the system as a function of its two parameters: the radii R_Y of its constituent tripoles and the orbital radius R_e.

Preprints (www.preprints.org) | NOT PEER-REVIEWED | Posted: 25 December 2023 doi:10.20944/preprints202312.0679.v2

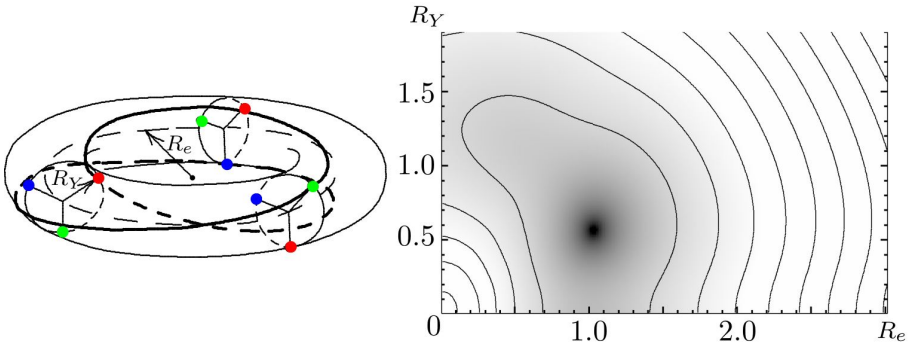

Figure 11. *Left:* scheme of the loop-closed trajectories of colour-charges in a system formed of three like-charged tripoles Y. *Right:* equilibrium potential as calculated by varying two parameters of the system – the radii R_Y of the system's tripole constituents, and radius R_e of their common ring-closed orbit (the radii are expressed in units of $l_\circ$).

The equilibrium potential above is calculated for the simplest static case, for which the ratio $q = R_e/R_Y$ between the radius of the tripole's common orbit and the tripole's radius is quite small, as $R_e \approx 1$ and $R_Y \approx 0.5$. Thus, $q \approx 2$. However, this system cannot be static: presumably, its constituents move with high speed along their common orbit. Thence, due to the centrifugal force, the actual ratio q is larger (a more detailed study of this specific case [38] suggests that $q \approx 15$).

An important feature of this system is that the path of each colour charge belonging to a particular tripole overlaps exactly with the paths of two other colour charges that belong to two other tripoles whose colour charges are complementary to the colour charge of the first. As an example, the path of the green-colour charge of one of the constituent tripoles (say, the first) is indicated on the left panel of Figure 11 by the black Smale-Williams curve which is traced along the torus towards the red-colour charge of the third tripole and then to the blue-colour charge of the second tripole. That is, the colour-currents that constitute this structure are dynamically colourless. Averaged in time, the exterior field of this particle has only two polarities corresponding to the conventional electric field. So, this system is *colour neutral*, which means that it can interact only with other colour-neutral systems via their electric fields.

By its properties, this system matches a fundamental fermion called *the electron*, although the standard-model electron is a point-like particle, with its properties (mass, charge, spin, gyromagnetic ratio, etc.) being defined quantum-mechanically without self-sufficing reasons. The properties of the above-described composite electron emerge naturally due to the symmetries of elliptical space.

The photon.

In this ansatz, one can envisage yet another colour-neutral composite system. It is formed of two unlike-charged tripoles, Y^+Y^-. It is very similar to the above described system Y^+Y^+ of like-charged particles shown in Figure 9, except for the electric-field sign change for one of its two constituents – from repulsion to attraction. Consequently, the minimum of the potential energy of this system is achieved near the origin, as shown on the right panel of Figure 12. In the calculation scheme for this system (shown on the left panel of Figure 12), the graphical [r,g,b]-colours denoting the colour-charges of the negatively charged constituent Y^- are replaced with the complementary colours [cyan, magenta and yellow] – to highlight the distinction between the positive and negative electric charges.

Preprints (www.preprints.org) | NOT PEER-REVIEWED | Posted: 25 December 2023 doi:10.20944/preprints202312.0679.v2

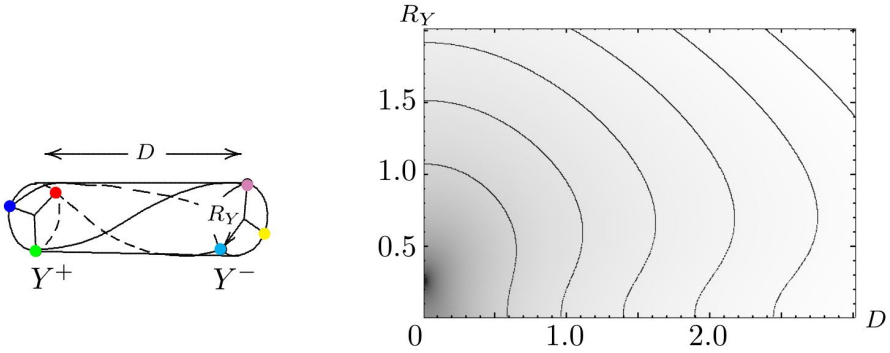

Figure 12. Potential energy of a string formed of two unlike-charged tripoles Y^+ and Y^- separated by distance D and with their radii R_Y (darker shades correspond to lower potentials).

Both electric- and colour-field components of this structure are almost entirely cancelled. Therefore, it has almost zero mass and moves with the maximal available speed. If disturbed by a strong external field, the structure Y^+Y^- can be polarised, with the distance between its constituents being increased and its field converted to a dipole field. Along its path, this dipole will be spinning with a frequency proportional to the energy of its initial disturbance, which also determines the frequency of the associated electric and magnetic fields. Within this framework, the structure Y^+Y^- by its properties is identifiable as the photon.

While not disturbed, the photons Y^+Y^- have zero or very small energy (frequency). Such zero-energy photons can populate the entire space mimicking the physical vacuum, the latter is, indeed, known as a polarisable medium. According to our ansatz, this medium represents a physical realisation of elliptical space, which, on one side, determines the properties of the entire Universe, and, on the other side, gives rise to the variety of matter particle species.

4. Discussion

I present two examples of possible observational consequences of the main feature of elliptical space adopted by the standard cosmological model, on the assumption that this provides the explanation of the origin of fundamental particles. The first example (§ 3.1) relates the cosmological redshifts of remote sources to their distances from an observer. The second example (§ 3.2) deals with the same topological structure of space but on the microscopic scale.

4.1. Cosmological scale

It turns out that, on the large scale, the redshift-distance relationship matches the observed relationship between the redshifts and distances of the type Ia supernova (the "standard candles" of modern observational cosmology). The goodness-of-fit parameter, χ^2, of the theoretical distance moduli calculated for elliptical space compared with the observed distance moduli of the type Ia supernovae is approximately the same as the χ^2 calculated for the standard cosmological model ΛCDM.

This suggests that two different explanations of the possible origin of spectral line shifts in remote galaxy spectra given by these two different models are equivalent in practical terms (at least, for the available redshift range of the type Ia supernovae discovered so far). One explanation (given by ΛCDM) rests upon the idea of accelerated recession of galaxies, and another is based on Einstein's prediction of gravitational redshift. The similarity with which they match observational data evokes the Einstein's equivalence principle between acceleration and gravity.

So far, there is no disagreement between the hypothesised physical structure of elliptical space and observational data. However, further observational evidence is required, and this is expected to come from the most powerful telescopes, such as the James Webb Space Telescope (JWST) or the

Preprints (www.preprints.org) | NOT PEER-REVIEWED | Posted: 25 December 2023 doi:10.20944/preprints202312.0679.v2

Extremely Large Telescope under construction in Chile. The discovery of type-Ia supernovae beyond redshifts $z \sim 2.3$ might confirm or disprove the presented hypothesis.

As we have seen in §3.1, the SdS and ΛCDM models are equivalent for the redshifts within the range $0 < z < 2.3$, as their goodness-of-fit χ^2 criteria are practically identical. But for larger redshifts, these two models diverge (see the right panel of Figure 3). According to this scenario, if newly-discovered high-redshift supernova appear dimmer than what is predicted for them by the ΛCDM model, then the SdS metric of elliptical space would need to be considered more seriously.

4.2. Microscopic scale

In the past, some attempts to address the question why we have this particular set of fundamental particles (the electron, the photon, quarks, etc.) were made by string theorists [39,40] and researchers working on composite theories of particles [41–43]. Unfortunately, none of those attempts succeeded, although some correspondence with experimental data was found when exploring potentials similar to those discussed in §3.2.4. For example, Chan and Tsou in 2002 introduced a potential with a dual SU(3) symmetry [44]. By adjusting three free parameters of their model the authors were able to reproduce the experimentally determined quark mass ratios (the Cabbibo-Kobayashi-Maskawa matrix).

The physical interpretation of the topological structure of elliptical space discussed here in terms of the connectivity between points separated by large distances via Einstein-Rosen bridges (microscopic wormholes) leads to a symmetry that topologically determines a unique set of allowable self-assembling clusters of microscopic wormholes. Their properties match the observed set of elementary particles. Here we have discussed just the simplest of these clusters whose properties match the properties of the electron and the photon. Other possibilities are discussed elsewhere [45].

The order in which tripolar charges self-assemble and form clusters is important. For instance, the order of colour charges in the closed-loop structure shown in Figure 11 (the electron) makes these charges move along their shared trajectories. As discussed, this renders the structure dynamically colourless, because all its internal colour-polarities alternate consecutively at each point of their trajectories with a high frequency. By being electrically like-charged and dynamically colourless, a pair of such closed-loop structures (a pair of electrons) should repel each other, as is well known. However, under certain circumstances at low temperatures, if the orbital frequencies of their constituents are synchronised, the residual colour (strong-like) fields overcome the repulsion, and these closed-loop structures (the electrons) are able to combine pair-wisely, or even to form a regular grid of paired electrons. One can devise an experimental set-up to verify this prediction. So, in principle, the proposed hypothesis can be experimentally verified on the microscopic scale, as well as the cosmological scale.

5. Conclusions

Elliptical space was adopted some time ago as the basis for the standard cosmology. But its main, although unusual, property – the identification of its antipodal points – has so far escaped the attention of researches. I have tried to draw the attention of cosmologists and particle physicists to this property of elliptical space by showing that its physical interpretation in the form of short-circuiting of its largely separated points via microscopic wormholes can be used to build models on both cosmological and microscopic scales that match observational and experimental data. The match on the cosmological scale is of the same level of accuracy as of the standard cosmological model. Meanwhile, the latter is currently experiencing severe problems due to the emerging observational evidence from the JWST that the standard model's prediction with respect to the age of the Universe is largely incorrect [47–50]. The model discussed can resolve this dilemma.

Funding: This research received no external funding.

Institutional Review Board Statement: Institutional ethical review and approval are not applicable to this study, as it does not involve animals or humans.

Informed Consent Statement: Not applicable.

Data Availability Statement: The data used for preparing this manuscript are available at https://pantheonplussh0es.github.io.

Acknowledgments: This research has made use of the following archive: The *Pantheon+* Type Ia supernova distance moduli from [13,46] I am also acknowledging the use of the cosmoFns software package developed by Andrew Harris and available at the following web page: github.com/cran/cosmoFns. I would like to thank Dr Paul Kuin, Dr Leslie Morrison, Dr Alice Breeveld, Dr. Victor Tostykh and Prof. Mat Page for useful discussions on the matters in this paper.

Conflicts of Interest: The author declares no conflict of interest.

Abbreviations

The following abbreviations are used in this manuscript:

FLRW	Friedmann-Lemaitre-Robertson-Walker (metric)
JWST	James Webb Space Telescope
ΛCDM	Lambda-Cold-Dark-Matter (cosmological model)
dS	de Sitter (metric)
SdS	Schwarzschild-de Sitter (metric)

References

1. Hamilton, W.R. On quaternions; or on a new system of imaginaries in algebra, *Philosophical Magazine Series 3* **1844**, XXV, 10–13, 241–246, DOI: 10.1080/14786444408644923.
2. de Sitter, W. On Einstein's theory of gravitation, and its astronomical consequences. Third paper, *MNRAS* **1917**, *78*, 3–28. DOI: 10.1093/mnras/78.1.3.
3. Einstein, A. Kosmologische betrachtungen zur allgemeinen Relativitätstheorie, *Sitz.Preuss.Akad.Wiss Phys.* **1917**, *VL*, 142–152.
4. Newcomb, S. Elementary theorems relating to the geometry of a space of three dimensions and of uniform positive curvature in the fourth dimension, *J. für die reine und angewandte Mathematic* **1877**, *LXXXIII*, 293–299.
5. Schwarzschild K., Ueber das zulässige Krümmunsmass des Raumes, *Vierteljahrssch. der Astr. Ges.* **1900**, XXXV, 337-347.
6. Lemaître, G. Un univers homogène de masse constante et de rayon croissant rendant compte de la vitesse radiale des nébuleuses extra-galactiques, *Ann. Soc. Sci. Bruxelles A.* **1927**, *47*, 49–59.
7. Tolman, R.C. On the estimation of distances in a curved universe with a non-static line element. *Proc. Nat. Acad. Sci. USA* **1930**, *16*, 511–520. DOI: 10.1073/pnas.16.7.511.
8. Robertson, H.P. Kinematics and world structure, *ApJ* **1935**, *82*, 284–301; *ApJ* **1936**,*83*, 187–201, 257–271. DOI: 10.1086/143681
9. Hubble, E., A relation between distance and radial velocity among extragalactic nebulae, *Proc. Natl. Acad. Sci.* **1929**, *15*, 168–173. DOI: 10.1073/pnas.15.3.168.
10. Friedmann, A. Über die Krümmung des Raumes, *Zeitschrift für Physik A* **1922**, *10*, 377–386. DOI: 10.1007/BF01332580.
11. Walker, A.G. On Milne's theory of world-structure, *Proc. Lond. Math. Soc.* Ser. 2, **1937**, *42*, 90–127; DOI: 10.1112/plms/s2-42.1.90.
12. Haradhan K. M., A Brief Analysis of de Sitter Universe in Relativistic Cosmology, J. Sci. Achiev. **2017**, *2*, 1-17.
13. Brout, D., Scolnic, D., Popovic, B., Riess, A.G., Zuntz, J., Kessler, R., Carr, A., Davis, T. M., et al., The Pantheon+ Analysis: Cosmological Constraints, *ApJ* **2022**, *938*, 110 (24pp). DOI: 10.3847/1538-4357/ac8e04.
14. Tamburini, F., Licata, I., General relativistic wormhole connections from Planck-scales and the ER = EPR conjecture, *Entropy* **2020**, *22*, 3 (14 pp.). DOI: 10.3390/e22010003.
15. Morris, M.S., Thorne, K.S., Wormholes in spacetime and their use for interstellar travel: A tool for teaching general relativity, *Am. J. Phys.* **1988**, *56*, 395–412. DOI: 10.1119/1.15620.
16. Einstein, A. and Rosen, N. The Particle Problem in the General Theory of Relativity, *Phys. Rev.* **1935**, *48*, 73–77. DOI: 10.1103/PhysRev.48.73.
17. Morris, M.S., Thorne, K.S., Yurtsever, U., Wormholes, time machines, and the weak energy condition, *Phys. Rev. Lett.* **1988**, *61*, 1446–1449. DOI: 10.1103/PhysRevLett.61.1446.

18. Tolman, R.C. Static solutions of Einstein's field equations for spheres of fluid. *Phys. Rev.* **1939**, *55*, 364–373. DOI: 10.1103/PhysRev.55.364.
19. Wheeler J.A., Geons, *Phys. Rev.* **1955**, *97*, 511-536. DOI: 10.1103/PhysRev.97.511.
20. Misner C. & Wheeler J.A., Classical physics as geometry, *Ann. Phys.* **1957**, *2*, 525–603. DOI: 10.1016/0003-4916(57)90049-0
21. O.W. Greenberg, Spin and unitary spin independence in a paraquark model of baryons and mesons, Phys. Rev. Lett., 13, 598-602 (1964) DOI: 10.1103/PhysRevLett.13.598.
22. Osenda O., Serra P., Tamarit F.A., Non-equilibrium properties of small Lennard-Jones clusters, **2002** Physica D - Nonlinear Phenomena, *168*, 336-340. DOI: 10.1016/S0167-2789(02)00521-3.
23. Osenda O., Tamarit F., Cannas S., Nonequilibrium structures and slow dynamics in a two-dimensional spin system with competing long-range and short-range interactions, Phys. Rev. E, **2009**, *80*, 21114-21127. https://doi.org/10.1103/PhysRevE.80.021114 DOI: 10.1103/PhysRevE.80.021114.
24. Lorentz H.A., The Theory of Electrons, 2nd Ed., (Teubner & Stechert, Leipzig, N.Y. **1916**, 344 pp.
25. Born M., On the quantum theory of the electromagnetic field, Proc. R. Soc. Lond. A 143, 410–437 (1934); DOI: 10.1098/rspa.1934.0010
26. Born M., Infeld L., Foundations of the new field theory, Proc. R. Soc. Lond. A 144, 425–451 (1934). DOI: 10.1098/rspa.1934.0059.
27. Dirac P.A.M., Classical theory of radiating electrons, Proc. R. Soc. Lond. A 167, 148–169 (1938) DOI: 10.1098/rspa.1938.0124.
28. Landau L.D., Lifshitz E.M., Field Theory, Rev. 2nd ed., Pergamon Press, Oxford, **1962**, 404 pp.
29. Frenkel J., On Born's theory of the electron, **1934**, Proc. R. Soc. Lond. A 146, 930. DOI: 10.1098/rspa.1934.0198.
30. Parker E.N., Cosmical Magnetic Fields, Clarendon Press, New York, **1979**, 841 pp.
31. Cox S.M., Matthews P.C., New instabilities in two-dimensional rotating convection and magnetoconvection, Physica D: Nonlinear Phenomena, **2001**, *149*, 210-229. DOI: 10.1016/S0167-2789(00)00204-9.
32. Pipin V.V., ,Kichatinov L.L., The solar dynamo and integrated irradiance variations in the course of the 11-year cycle, Astron. Rep., **2000**, *44*, 771-779. DOI: 10.1134/1.1320504.
33. Liu W., Haller G., Inertial manifolds and completeness of eigenmodes for unsteady magnetic dynamos, Physica D: Nonlinear Phenomena, **2004**, *194*, 297-319. DOI: 10.1016/j.physd.2003.03.002.
34. Kadomtsev B.B., Tokamak Plasma: A Complex Physical System, Inst. of Phys. Publ., Bristol, Philadelphia, **1992**, 208 pp.
35. Wesson J.A., Tokamaks, 2nd ed., Oxford Univ. Press, Oxford, **1997**, 680 pp.
36. White R.B., The Theory of Toroidally Confined Plasmas, revised 2nd ed., Imperial College Press, London, **2006**, 367 pp.
37. Kleman M., Lines and Walls, Wiley and Sons, Chichester, **1983**, 322 pp.
38. Yershov V. N., Quantum properties of a cyclic structure based on tripolar fields, **2007**, Physica D: Nonlinear Phenomena, 226, 136-143. DOI: 10.1016/j.physd.2006.11.009.
39. Witten E., **1996**, Bound states of strings and branes, Nucl. Phys. B, *460*, 335-350. DOI: 10.1016/0550-3213(95)00610-9
40. Polchinski J., String theory, Vol.1, Cambridge Univ. Press, Cambridge, **1998**, 422 pp.
41. Pati J.C., Salam A., Unified lepton-hadron symmetry and a gauge theory of the basic interactions, Phys. Rev. D, **1973**, *8*, 1240-1251. DOI: 10.1103/PhysRevD.8.1240.
42. Harari H., Seiberg N.A., **1979**, A schematic model of quarks and leptons, Phys. Lett. B, *86*, 83-86. DOI: 10.1016/0370-2693(79)90626-9.
43. Kalman C.S., **2005**, Why quarks cannot be fundamental particles, Nuct. Phys. B - Proc. Suppl., *142*, 235-237. DOI: 10.1016/j.nuclphysbps.2005.01.042.
44. Chan H.M., Tsou S.T., Fermion generations and mixings from dualized Standard Model, **2002** Acta. Phys. Polon. B, , *33*, 4041-4100.
45. Yershov, V.N., Neutrino masses and the structure of the weak gauge boson, in Focus on Boson Research, Ed. A.V. Ling, Nova Science Publishers (Hauppauge NY), **2006**, 131-181.
46. Scolnic, D., Brout, D., Carr, A., Riess, A.G., Davis, T.M., Dwomoh, A., Jones, D.O., Ali, N., Charvu, P., et al., The Pantheon+ Analysis: The Full Dataset and Light-Curve Release, *ApJ* **2022**, *938*, 113 (15pp). DOI: 10.3847/1538-4357/ac8b7a.

47. Lovyagin N., Raikov A., Yershov V., Lovyagin Yu., Cosmological model tests with JWST, Galaxies, **2022**, 10, 108 (20 pp). DOI: 10.3390/galaxies10060108.
48. Castellano, M., Fontana A., Treu T., Merlin E., Santini P., Bergamini P., Grillo C., Rosati P., et al., Early results from GLASS-JWST. XIX. A high density of bright galaxies at $z \approx 10$ in the A2744 region, **2023**, ApJ Lett., *948*, L14 (11pp).
DOI: 10.3847/2041-8213/accea5.
49. Gupta R.P., JWST early Universe observations and ΛCDM cosmology, **2023**, MNRAS, *524*, 3385–3395.
DOI: 10.1093/mnras/stad2032.
50. Melia F., The cosmic timeline implied by the JWST high-redshift galaxies, **2023**, MNRAS, *521*, L85-L89.
DOI: 10.1093/mnrasl/slad025.